










## Probing intrinsic magnetization dynamics of the $\text{Y}_3\text{Fe}_5\text{O}_{12}/\text{Bi}_2\text{Te}_3$ interface at low temperature

A. R. Will-Cole <sup>1,2,\*</sup>, Valeria Lauter,<sup>3</sup> Alexander Grutter <sup>4</sup>, Carsten Dubs <sup>5</sup>, David A. Lidsky,<sup>2,6</sup> Morris Lindner,<sup>5</sup> Timmy Reimann,<sup>5</sup> Nirjhar Bhattacharjee,<sup>1</sup> Tzu-Ming Lu,<sup>2,6</sup> Peter Sharma <sup>2</sup>, Nichole R. Valdez <sup>2</sup>, Charles J. Pearce <sup>2</sup>, Todd C. Monson <sup>2</sup>, Matthew Matzelle <sup>7</sup>, Arun Bansil,<sup>7</sup> Don Heiman,<sup>7,8</sup> and Nian X. Sun <sup>1,†</sup>

<sup>1</sup>Department of Electrical and Computer Engineering, *Northeastern University*, Boston, Massachusetts 02115, USA

<sup>2</sup>Sandia National Laboratories, Albuquerque, New Mexico 87123, USA

<sup>3</sup>Neutron Scattering Division, Neutron Sciences Directorate, *Oak Ridge National Laboratory*, Oak Ridge, Tennessee 37831, USA

<sup>4</sup>Center for High Resolution Neutron Scattering, *National Institute of Standards and Technology*, Gaithersburg, Maryland 20878, USA

<sup>5</sup>INNOVENT e.V. Technologieentwicklung, Prüssingstrasse 27B, 07745 Jena, Germany

<sup>6</sup>Center for Integrated Nanotechnologies, *Sandia National Laboratories*, Albuquerque, New Mexico 87123, USA

<sup>7</sup>Department of Physics, *Northeastern University*, Boston, Massachusetts 02115, USA

<sup>8</sup>Plasma Science and Fusion Center, *Massachusetts Institute of Technology*, Cambridge, Massachusetts 02139, USA



(Received 11 December 2023; revised 4 April 2024; accepted 1 July 2024; published 23 July 2024)

Topological insulator–magnetic insulator (TI–MI) heterostructures hold significant promise in the field of spintronics, offering the potential for manipulating magnetization through topological surface state–enabled spin-orbit torque. However, many TI–MI interfaces are plagued by issues such as contamination within the magnetic insulator layer and the presence of a low-density transitional region of the topological insulator. These interfacial challenges often obscure the intrinsic behavior of the TI–MI system. In this study, we addressed these challenges by depositing sputtered  $\text{Bi}_2\text{Te}_3$  on liquid phase epitaxy grown  $\text{Y}_3\text{Fe}_5\text{O}_{12}/\text{Gd}_3\text{Ga}_5\text{O}_{12}$ . The liquid phase epitaxy grown  $\text{Y}_3\text{Fe}_5\text{O}_{12}$  has been previously shown to have exceptional interface quality, without an extended transient layer derived from interdiffusion processes of the substrate or impurity ions, thereby eliminating rare-earth impurity-related losses in the MI at low temperatures. At the TI–MI interface, high-resolution depth-sensitive polarized neutron reflectometry confirmed the absence of a low-density transitional growth region of the TI. By overcoming these undesirable interfacial effects, we isolate and probe the intrinsic low-temperature magnetization dynamics and transport properties of the TI–MI interface. Our findings revealed strong spin pumping at low temperatures, accompanied by an additional in-plane anisotropy. The enhanced spin pumping at low temperatures is correlated with the observed suppression of bulk conduction and the weak antilocalization in the TI film, highlighting the interplay between the transport and spin pumping behavior in the TI–MI system.

DOI: [10.1103/PhysRevMaterials.8.074409](https://doi.org/10.1103/PhysRevMaterials.8.074409)

### I. INTRODUCTION

The unique electronic band structure of a topological insulator consists of topologically protected Dirac surface states (TSS) which enable two-dimensional metallic surface states while the bulk is insulating [1–3]. Three-dimensional topological insulators (TIs) include  $\text{Bi}_{1-x}\text{Sb}_x$  alloys and hexagonal  $X_2Q_3$  compounds ( $X = \text{Bi}, \text{Sb}, \text{Bi}_{1-x}\text{Sb}_x$ ;  $Q = \text{Se}, \text{Te}$ ). While  $\text{Bi}_{1-x}\text{Sb}_x$  alloys have complex surface states, the  $\text{Bi}_2\text{Se}_3$  family compounds with tetradymite crystal structure have simple, robust surface states with a single Dirac cone at the  $\Gamma$  point [4,5]. A physical signature of TIs, though a property not limited to TI materials, is spin-momentum locking, i.e., the carrier electron spin in the TSS is perpendicularly locked to its momentum. Therefore, an injected charge current will become spin polarized in a TI [6–8]. This property has been confirmed with angle-resolved photoemission spectroscopy [9], polarized optical spectroscopy [10], and via direct electrical

detection [8]. These electronic properties enable manipulation of magnetization through the application of spin-orbit torque (SOT) via a spin-polarized current. TI SOT efficiencies ( $\theta_{\text{SOT}}$ ) are much higher than heavy metals [11–15], and this high  $\theta_{\text{SOT}}$  of TIs allows for a lower critical current density for magnetization switching ( $\sim 10^5\text{--}10^6$  A/cm<sup>2</sup>) compared with heavy metals (one to two orders of magnitude smaller in the case of TI). This makes TI–magnetic insulator (MI) interfaces critically important for future, low-power spintronics memory and logic devices [16].

Interfaces between TIs and MIs exhibit interesting transport behaviors, including the anomalous Hall effect (AHE) which is often attributed to a magnetic proximity effect (MPE), also known as proximity-induced magnetization (PIM). Complex oxides, such as yttrium iron garnet (YIG), are of intense interest in this context due to their insulating nature, low magnetic losses, and tunable magnetic ground state. Although the AHE has been experimentally observed in TI/oxide systems such as  $\text{Bi}_2\text{Se}_3/\text{Y}_3\text{Fe}_5\text{O}_{12}$  [17],  $\text{Bi}_2\text{Se}_3/\text{LaCoO}_3$  [18],  $(\text{Bi}_x\text{Sb}_{1-x})_2\text{Te}_3/\text{Y}_3\text{Fe}_5\text{O}_{12}$  [19], and  $(\text{Bi}_x\text{Sb}_{1-x})_2\text{Te}_3/\text{Tm}_3\text{Fe}_5\text{O}_{12}$  [20], the AHE magnitude ( $R_{\text{AHE}}$ )

\*Contact author: arwillc@sandia.gov

†Contact author: n.sun@northeastern.edu

of YIG-based bilayers is two to three orders of magnitude smaller than all telluride-based van der Waals heterostructures, respectively [19,21]. Further, it must be noted that while YIG/heavy metal interfaces (i.e., YIG/Pt) yield a robust AHE [22], the AHE persists even in Pt/Cu/YIG trilayers, where a Cu layer is deliberately inserted to eliminate the MPE (known as nonlocal AHE) [23,24]. Nevertheless, there are several reports of significant spin pumping in TI/YIG heterostructures [25–27], thus it is critical to directly probe depth and element-resolved magnetization profiles to fully understand these interfaces. To that end, polarized neutron reflectometry (PNR) and x-ray magnetic circular dichroism, have been employed to search for PIM. A MPE has been experimentally observed with PNR in several MI–TI systems, including EuS/V-doped  $\text{Sb}_2\text{Te}_3$  [28], EuS/ $\text{Bi}_2\text{Se}_3$  [29], EuS/ $(\text{Bi}_{0.2}\text{Sb}_{0.8})_2\text{Te}_3$  [30], and  $\text{Cr}_2\text{Ge}_2\text{Te}_6/(\text{Bi}, \text{Sb})_2\text{Te}_3/\text{Cr}_2\text{Ge}_2\text{Te}_6$  [31].

Despite this progress and the overwhelming interest in TI–MI heterostructures, recent literature has struggled to access the intrinsic properties of the TSS at a magnetic interface due to unique interfacial defects prevalent in most TI-based MPE/PIM heterostructures. Specifically, there are typically two features in TI–MI systems that confound the intrinsic interfacial behavior: (1) chemically inhomogeneous transient layers in the magnetic insulator at the magnetic insulator-substrate interface and (2) a low-density, intergrowth region of the TI at the TI–MI interface. With respect to the well-studied magnetic insulator-substrate interface of  $\text{Y}_3\text{Fe}_5\text{O}_{12}/\text{Gd}_3\text{Ga}_5\text{O}_{12}$  (YIG/GGG), extended intermixed, nonstoichiometric interface layers in the magnetic insulator (up to 10 nm) leads to significantly higher ferromagnetic resonance linewidth at low temperatures due to slowly relaxing impurities within the YIG film [32–36]. These transient layers can result in a magnetic dead layer or antiparallel magnetization at sputtered YIG/GGG interfaces, as observed by superconducting quantum interference device magnetometry and PNR [33,34]. The second feature common to TI–MI heterostructures—a low-density, intergrowth region of the TI at the TI–MI interface—has been observed with PNR in several systems such as  $\text{Bi}_2\text{Se}_3/\text{MgAl}_{0.5}\text{Fe}_{1.5}\text{O}_4$  [37] and  $\text{Bi}_2\text{Se}_3/\text{Y}_3\text{Fe}_5\text{O}_{12}$  [38]. In this work, we seek to understand the intrinsic interface-driven phenomenon of the  $\text{Bi}_2\text{Te}_3/\text{YIG}$  system while minimizing the effect of such extrinsic factors. We mitigate the YIG/GGG contamination by employing liquid phase epitaxy (LPE) –grown YIG on GGG. LPE-grown YIG has been demonstrated to have nearly perfect microstructure, a chemically sharp interface, and negligible magnetic losses at low temperatures due to suppressed YIG/GGG interdiffusion [39–42]. Further, we employ RF magnetron sputtering deposition to deposit  $\text{Bi}_2\text{Te}_3$  onto the YIG and use PNR to show that a low-density transitional growth regime is not present at the  $\text{Bi}_2\text{Te}_3$  (BT)/YIG interface. Specifically, we grew 25-nm-thick  $\text{Bi}_2\text{Te}_3$  at 250 °C or at 25 °C via RF magnetron sputtering on 50-nm-thick liquid phase epitaxy grown  $\text{Y}_3\text{Fe}_5\text{O}_{12}$  on  $\text{Gd}_3\text{Ga}_5\text{O}_{12}$  substrates. Representative x-ray diffraction and atomic force microscopy can be found in the Supplemental Material [43]. While other studies have been conducted on the low-temperature magnetization dynamics of TI–MI heterostructures, i.e.,  $\text{Bi}_2\text{Se}_3/\text{YIG}$  [26,27],

our BT/YIG system is uniquely situated to isolate and probe the intrinsic interaction between the TSS and magnetic insulator due to the absence of the aforementioned features that can confound the true physical behavior of the TI–MI interface. Thus, we used PNR, magnetotransport measurements, and magnetization dynamics to elucidate the interplay between MPE, spin pumping, and the TI TSS.

## II. POLARIZED NEUTRON REFLECTOMETRY

To investigate the quality of the BT/YIG interface and the presence of a possible magnetic proximity effect we performed PNR using the Magnetism Reflectometer at the Spallation Neutron Source at Oak Ridge National Laboratory [44]. PNR is sensitive to the depth profiles of the nuclear (real  $\rho_N$  and imaginary  $\rho_{N,i}$ ) and magnetic ( $\rho_M$ ) scattering length densities (furthermore referred to as the nuclear SLD and magnetic SLD, respectively) of the heterostructure. The nuclear SLD is determined by the density and composition of the scattering material, while the magnetic SLD is directly related to the net in-plane magnetization. Simultaneous depth-resolved information about the heterostructure composition, density, and magnetization can therefore be obtained by fitting the PNR data [45,46], making it an ideal technique for interrogating the BT/YIG interface. Measurements were conducted in a closed cycle refrigerator equipped with an electromagnet. For the PNR measurement, a spin-polarized neutron beam with a wavelength band  $\lambda$  (2.5–8.5 Å) was incident on the sample at a grazing incidence angle  $\theta$ , while a spin flipper was used to alternate the incoming neutron spin state. The spin-dependent neutron reflectivity spectra,  $R+$  and  $R-$ , were measured as a function of the wavevector transfer,  $Q = 4\pi \sin(\theta)/\lambda$ , along the direction normal to the film surface. The measurements were collected at 100 K first, and then the sample was field-cooled down to 10 K in an applied, in-plane magnetic field of 0.5 T, where the second measurement was performed. For these measurements, the samples were first measured at remanence (0.005 T) and then a measurement was taken at saturation in a field of 0.5 T, far exceeding the saturation field of the sample of <0.5 mT. PNR samples were fabricated with an 8 mm × 8 mm cross-sectional area to reduce the neutron count time required for the high- $Q$  measurements. The reflectivity data was fit using the REFLID software package as shown in Fig. 1 for measurements at 100 K and Fig. 2 for measurements at 10 K. Initially, our model included a disordered intergrowth region like that in Riddiford *et al.* [37], but the model layer converged to a zero thickness, and removing this layer from the model did not significantly alter the goodness of fit. This sharp transition in the nuclear SLD at the YIG/BT interface confirms the bilayer’s high-quality interface, which contrasts with the low-density, intergrowth region of the TI observed with PNR in the  $\text{Bi}_2\text{Se}_3/\text{MgAl}_{0.5}\text{Fe}_{1.5}\text{O}_4$  [37] and  $\text{Bi}_2\text{Se}_3/\text{Y}_3\text{Fe}_5\text{O}_{12}$  systems [38]. It is important to note that PNR and transmission electron microscopy have previously yielded consistent results with respect to these low-density, intergrowth TI regions—either both techniques have provided evidence of a transitional growth regime in the TI, or they both do not [31,37,38,47]. Therefore, PNR is a reliable, nondestructive method to assess the interface quality of TI heterostructures. The interfacial

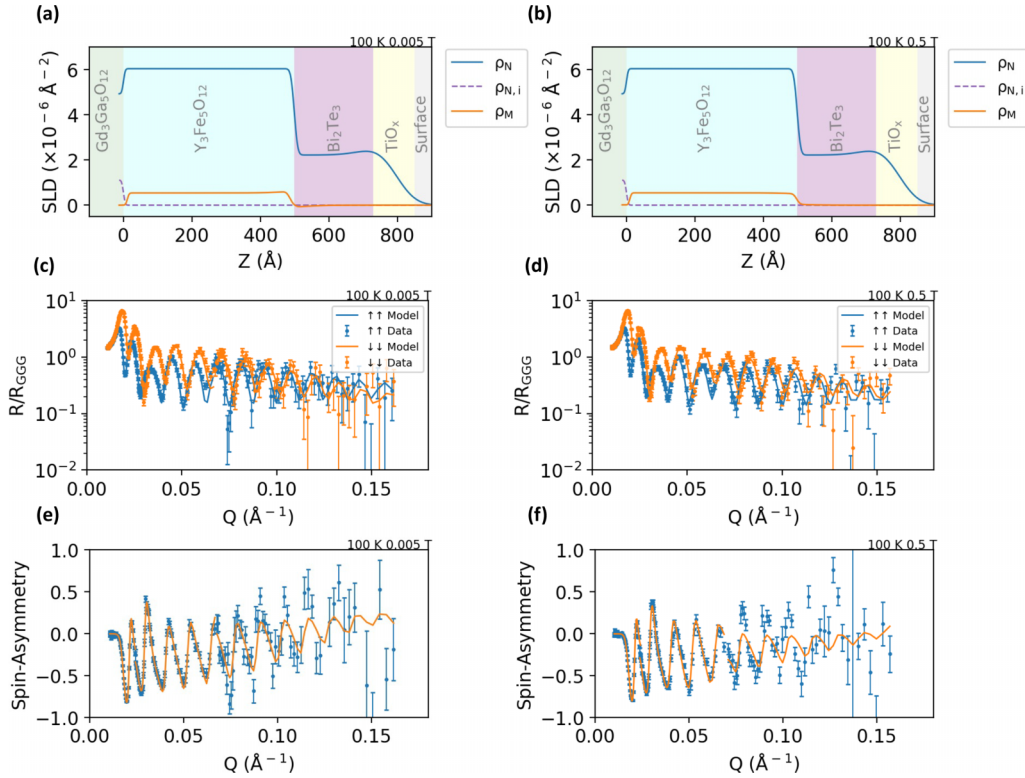


FIG. 1. Displayed are the model profiles for nuclear and magnetic scattering length density for measurements taken at 100 K with an in-plane bias field (a) 100 K and 0.005 T and (b) 100 K and 0.5 T, the reflectivity normalized by the theoretical reflectivity of a pure GGG substrate for both spin-up and spin-down neutrons along with their model fit for measurements taken at (c) 100 K and 0.005 T and (d) 100 K and 0.5 T, and the spin asymmetry along with the model fit for measurements taken at (e) 100 K and 0.005 T and (f) 100 K and 0.5 T. Error bars represent  $\pm 1$  standard deviation.

roughness between the YIG and  $\text{Bi}_2\text{Te}_3$  was fit at 8.18  $\text{\AA}$ . We did find that there is a region (approximately 11.3  $\text{\AA}$ ) at the YIG interface with the  $\text{Bi}_2\text{Te}_3$  with no net in-plane magnetization measured; the origin could either be canting out of plane at the BT/YIG interface due to interactions with the TSS, or this could be a true interfacial depletion region. We cannot differentiate between these two possibilities as our measurement geometry and analysis are only sensitive to in-plane magnetic moments. With respect to any induced magnetization in the TI, we did not find any conclusive evidence of PIM in the TI layer. In fact, the fitted magnetization values in the TI layer near the interface appear to fluctuate about zero, with three measurement conditions yielding small negative magnetizations while another converges to a small positive value as provided in Table I. Therefore, we conclude that the total moment induced in the  $\text{Bi}_2\text{Te}_3$ , if any, must be below the reliable detection limit of the PNR measurement. For more details about the fitted parameters, refer to the Supplemental Material [43].

### III. LOW-TEMPERATURE MAGNETOTRANSPORT MEASUREMENTS

To characterize the  $\text{Bi}_2\text{Te}_3$  transport behavior, we performed temperature and magnetic field-dependent transport measurements of the BT/YIG bilayer (250  $^\circ\text{C}$  grown BT/YIG bilayer) using a van der Pauw electrode geometry. Overall, our measurement observations are consistent with what has

been previously reported as standard for  $\text{Bi}_2\text{Te}_3$  films. From the ordinary Hall effect (OHE), as shown in Fig. 3(a), we observe a clear signature of  $n$ -type transport and we were able to extract the electron carrier concentration using  $n = 1/eR_H$ , where  $R_H = V_H d/B_z I_x$  and  $V_H$  is the Hall voltage,  $d$  is the film thickness,  $B_z$  is the magnetic flux density in the  $z$  direction (normal to the film),  $I_x$  is the current in the  $x$  direction (in the film plane), and  $e$  is the elemental charge of an electron. Then we calculated the electron carrier mobility at each temperature using  $\mu = R_H/\rho$ . Additional OHE measurements at additional temperatures up to room temperature can be found in the Supplemental Material [43]. As shown in Fig. 3(b), the electron carrier concentration decreases with reduced temperature. This is consistent with potential defect states near the Fermi level, so as the temperature is reduced there are fewer thermally excited carriers arising from these defect states. These defect states are likely due to Te vacancies and  $\text{Te}_{\text{Bi}}$  antisite defects as these contribute to  $n$ -type carrier conduction [48,49]. An increase in carrier mobility in Fig. 3(c) could also be expected at low temperatures due to reduced electron-phonon scattering. However, the observed increase in the mobility may be a result of multiband conduction. The longitudinal sheet resistivity in Fig. 3(d) shows metallic behavior and is consistent with the typical behavior of a highly doped degenerate semiconductor with a large carrier concentration—this metallic behavior has been previously reported for  $n$ -type  $\text{Bi}_2\text{Te}_3$  films [50]. Additionally, the longitudinal sheet resistivity is consistent with metallic behavior except for the upturn

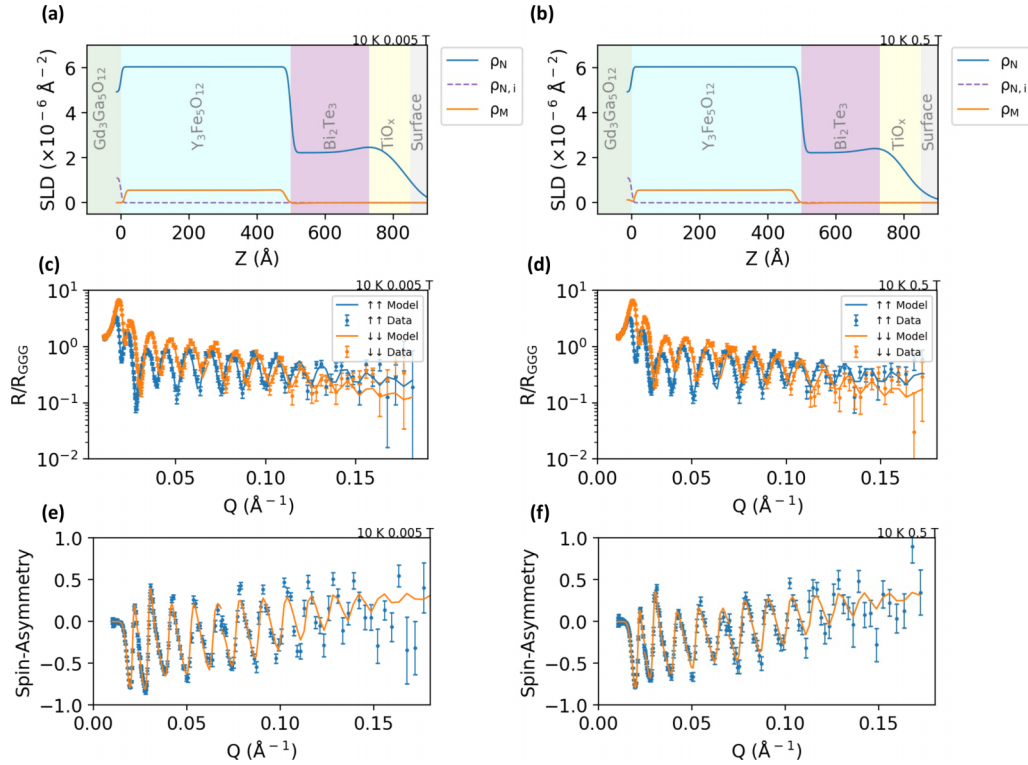


FIG. 2. Displayed are the model profile for nuclear and magnetic scattering length density for measurements taken at 10 K with an in-plane bias field (a) 10 K and 0.005 T and (b) 10 K and 0.5 T, the reflectivity normalized by the theoretical reflectivity of a pure GGG substrate for both spin-up and spin-down neutrons along with their model fit for measurements taken at (c) 10 K and 0.005 T and (d) 10 K and 0.5 T, and the spin asymmetry along with the model fit for measurements taken at (e) 10 K and 0.005 T and (f) 10 K and 0.5 T. Error bars represent  $\pm 1$  standard deviation.

at low temperature that may be due to the electron-electron interaction in two dimensions [51,52]. We measured the magnetoresistance from 3.5 to 20 K shown in Fig. 3(e). Below 15 K we observe the emergence of the quantum interference-associated weak-antilocalization (WAL) cusps in the low field regime, and at 15 K and above, the WAL cusps disappear and instead a quadraticlike dependence prevails in the low field regime. Below 15 K the magnetoresistance curves show a linear, nonsaturating magnetic field dependence above  $\sim 0.5$  T. At low temperature, TIs exhibit WAL due to the high conductivity and helical polarization of the TSS. It is worth noting, however, that observation of WAL is a necessary, but not sufficient condition to demonstrate the presence of the TSS in a TI film. Additionally, we do not observe any WAL suppression that normally accompanies a magnetic proximity effect in TI-magnetic heterostructures [53]. To reiterate, all these aforementioned transport behaviors are to be expected

for standard  $\text{Bi}_2\text{Te}_3$  films on substrates such as silicon, sapphire, etc. [48,50].

Typically, the transverse magnetoresistance signal consists of two components: the OHE and the AHE. As for effects other than the OHE, we do observe another Hall-like effect signature at low temperature shown in Fig. 3(f), and the methodology to separate this signal from the OHE signal can be found in the Supplemental Material [43], and follows the same methodology as found in Li *et al.* [54]. The onset of this nonlinear, saturating transverse resistance is below 15 K and the magnitude increases with decreasing temperature. This is consistent with what is often observed for the anomalous Hall effect since the anomalous Hall effect resistance should scale with the perpendicular component of the YIG magnetization. It is worth noting that the AHE response is typically observed in ferromagnetic metals and found in iron garnet films with strain-stabilized perpendicular magnetic anisotropy [55].

TABLE I. The PNR magnetic SLD results for the proximity-induced magnetization in the  $\text{Bi}_2\text{Te}_3$  near the YIG/ $\text{Bi}_2\text{Te}_3$  interface.

Measurement condition	$\rho_{M,\text{mean}} \times 10^{-6} \text{ \AA}^{-2}$	$\rho_{M,\text{best}} \times 10^{-6} \text{ \AA}^{-2}$	$\rho_M \times 10^{-6} \text{ \AA}^{-2}$ (95% confidence interval)
10 K and 0.005 T	-0.008(18)	-0.0148	[-0.043 to 0.028]
10 K and 0.5 T	$23(20) \times 10^{-3}$	0.0021	[-0.016 to 0.062]
100 K and 0.005 T	-0.158(20)	-0.1532	[-0.196 to -0.118]
100 K and 0.5 T	$-63(18) \times 10^{-3}$	-0.0595	[-0.097 to -0.027]

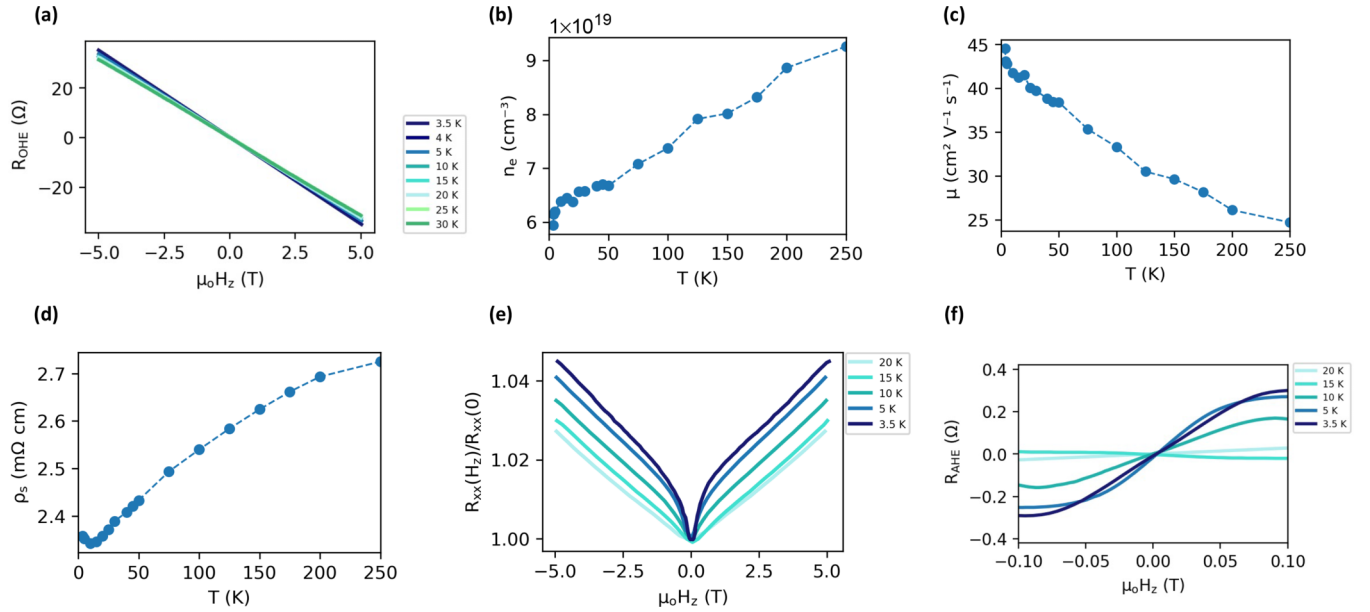


FIG. 3. Magnetotransport measurements for the 250 °C grown Bi<sub>2</sub>Te<sub>3</sub> on YIG/GGG. (a) Ordinary Hall effect component of the transverse resistance with an out-of-plane magnetic field. Measurements are shown for 3.5 K up to 250 K. (b) Displayed is the extracted electron carrier concentration as a function of temperature. (c) Displayed is the calculated carrier mobility as a function of temperature. (d) Longitudinal sheet resistivity in the absence of applied magnetic field. Measurements are shown for 3.5 K up to 250 K. (e) Longitudinal magnetoresistance. Measurements are shown for 3.5 K up to 20 K. (f) Transverse resistance with the ordinary Hall effect contribution removed. Measurements are shown for 3.5 K up to 20 K.

Similar effects have been observed in TI and heavy metals due to either magnetic proximity effects [29,54,56–58], the imaginary part of the spin mixing conductance at the interface (spin-Hall AHE) [59], or the spin-dependent scattering of the itinerant electrons with the magnetic interface (nonlocal AHE) [24]. It can be challenging to decouple the signatures interpreted as an AHE from the conduction of multiple carrier types as was reported in the Bi<sub>2</sub>Se<sub>3</sub>/MgAl<sub>0.5</sub>Fe<sub>1.5</sub>O<sub>4</sub> [37]. We assume that the nonlinear Hall component that we observe is due to the AHE as it does match the out-of-plane magnetization in terms of the observed saturation field, as shown in the Supplemental Material [43]. From Fig. 3(f) the AHE magnitude  $R_{\text{AHE}}$  is 0.30 Ω for our Bi<sub>2</sub>Te<sub>3</sub>/Y<sub>3</sub>Fe<sub>5</sub>O<sub>12</sub> bilayer at 3.5 K. This value is an order of magnitude higher than what has been previously reported for MBE-grown Bi<sub>2</sub>Te<sub>3</sub> on pulsed laser deposited YIG/GGG ( $R_{\text{AHE}} \approx 0.015$  Ω at 1.9 K) [19]; however, there could be minor differences between the interfacial quality, contact quality, film thicknesses, etc., though here we assume that the lack of the common transitional, low-density growth regime at the BT/YIG interface is responsible for our higher  $R_{\text{AHE}}$ . The AHE magnitude we find here is lower than that of (Bi<sub>0.16</sub>Sb<sub>0.84</sub>)<sub>2</sub>Te<sub>3</sub>/YIG ( $R_{\text{AHE}} \approx 1.71$  Ω)—the higher  $R_{\text{AHE}}$  in (Bi<sub>0.16</sub>Sb<sub>0.84</sub>)<sub>2</sub>Te<sub>3</sub>/YIG is expected due to Sb doping that suppresses the bulk conduction in the TI [19].

#### IV. LOW-TEMPERATURE MAGNETIZATION DYNAMICS

The aforementioned observations demonstrate that our BT/YIG heterostructure is an ideal platform to study the intrinsic TI–MI magnetization dynamics at low temperature. The high-quality BT/YIG interface, as confirmed by our PNR measurements, and our recent work on the liquid phase epi-

taxy grown YIG on GGG that shows high structural perfection at the YIG/GGG interface accompanied by low magnetic losses, finally permits the separation of the TSS effects from those detrimental interfacial defects [42]. We therefore performed temperature-dependent ferromagnetic resonance (FMR) measurements at 8 GHz on the bilayer of crystalline BT/YIG (BT  $T_{\text{growth}} = 250$  °C), and also on an amorphous BT/YIG bilayer (BT  $T_{\text{growth}} = 25$  °C). It is well established that spin pumping occurs in TI–MI systems [60]. It has also been shown that as the temperature is lowered and the TI bulk conduction is suppressed, that the spin pumping can become more pronounced (expressed experimentally as an increase in FMR linewidth). This has already been reported for the Bi<sub>2</sub>Se<sub>3</sub>/sputter-deposited YIG system which is influenced by rare-earth impurities in the film or by substrate elements that broaden the FMR linewidth at low temperatures [26,27]. In contrast, our BT/YIG system has minimal effects from rare-earth impurities in the film and negligible interdiffusion of the substrate elements [42]. We observe FMR linewidth broadening at low temperatures [displayed in Figs. 4(a) and 4(b)], and we attribute this to the fact that spin pumping becomes more dominant at low temperatures due to the TI TSS, which is consistent with our magnetotransport results that indicate the suppression of the bulk conduction states. There is approximately a tenfold enhancement of the FMR linewidth at 10 K in the BT/YIG compared to the YIG reference film. At 10 K we performed frequency-dependent FMR, which can be found in the Supplemental Material [43], and calculated the Gilbert damping parameters for YIG/GGG and BT (BT  $T_{\text{growth}} = 250$  °C)/YIG/GGG is  $2 \times 10^{-4}$  and  $9.9 \times 10^{-3}$ , respectively—a significant increase of the Gilbert damping parameter in the bilayer of crystalline BT/YIG). There was

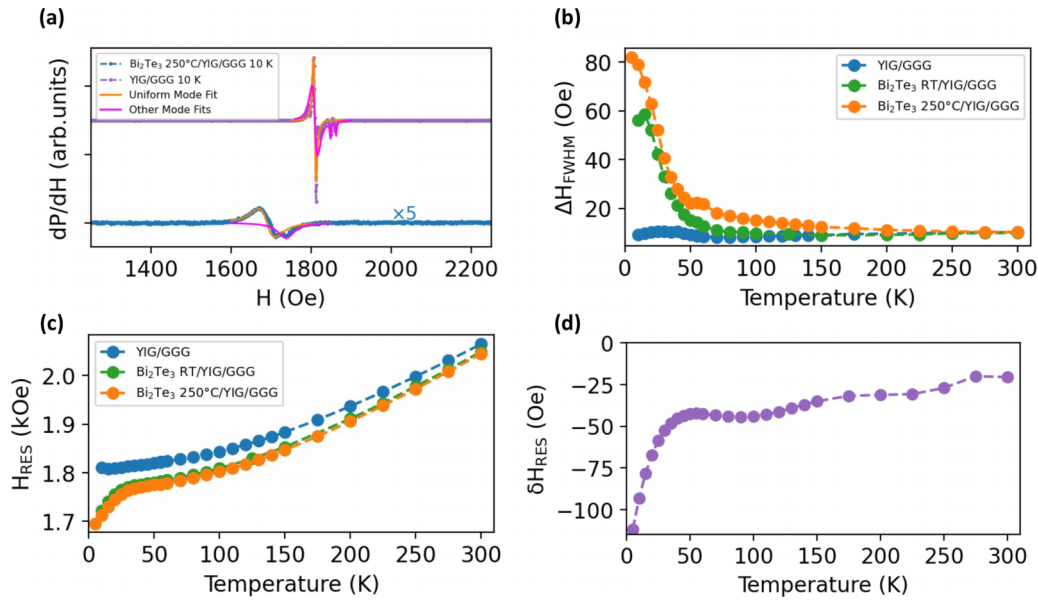


FIG. 4. (a) Representative FMR spectra at 8 GHz at 10 K of the  $250^\circ\text{C}$  grown BT/YIG/GGG film and YIG/GGG reference sample. The uniform mode and additional spin wave modes are both fitted with a Lorentzian. (b) The uniform FMR mode full width at half maximum linewidth at 8 GHz as a function of temperature for the YIG/GGG reference film and sputtered  $\text{Bi}_2\text{Te}_3$  films deposited at  $250^\circ\text{C}$  or room temperature on the YIG/GGG substrate. (c) The uniform FMR mode resonance field at 8 GHz as a function of temperature for the YIG/GGG reference film and the sputtered  $\text{Bi}_2\text{Te}_3$  films deposited at  $250^\circ\text{C}$  or room temperature on the YIG/GGG substrate. (d) The difference curve of the uniform FMR mode resonance field at 8 GHz for the YIG film/GGG reference sample and BT/YIG /GGG substrate deposited at  $250^\circ\text{C}$ . Note that  $1 \text{ Oe} = 10^3/(4\pi) \text{ A/m} = 0.1 \text{ mT}$ .

also an increase in the inhomogeneous broadening between the samples, which we believe may be due to inhomogeneities in the through thickness anisotropy due to interfacial exchange coupling to the TI TSS; however, this requires more in-depth study of thickness dependence to fully elucidate. With respect to changes in the film anisotropy, we also observe a large, induced in-plane magnetic anisotropy for the BT/YIG compared with the YIG reference film evident by the uniform FMR mode shift to a lower resonance field, which can be seen in Figs. 4(a), 4(c), and 4(d). A shift to a lower resonance field can only occur if there is either a change in anisotropy or in the magnetization of the film. As shown in the Supplemental Material [43], the magnetization of the YIG/GGG is consistent with that of the BT/YIG/GGG, therefore we qualitatively attribute the significant resonance field shift to additional easy-plane anisotropy using a similar rationale as by Liu *et al.* [27]. Overall, this finding contrasts with what has been reported in the  $\text{Bi}_2\text{Se}_3/\text{YIG}$  system by Fangchiang *et al.* who discussed in-plane anisotropy with some competing out-of-plane anisotropy at lower temperatures, while Liu *et al.* reported a clear additional out-of-plane anisotropy [26,27]. However, at room temperature Tang *et al.* experimentally found an additional easy-plane anisotropy for the YIG/ $(\text{Bi}_x\text{Sb}_{1-x})_2\text{Te}_3$  TI films [25]. Based on the arguments of Tang *et al.*, the direction of spins pumped into the TSS via FMR must be locked in the plane when the TSS are dominant in the TI layer. Since the spins in the TI and the YIG are exchange coupled across the YIG/TI interface, the precessing spins of the YIG are forced to align with the spins pumped into the TSS such that they are locked in the plane of the interface. Hence, spin pumping into the TSS creates not only a significant damping effect on the magnetization precession, but also an added easy-plane

or in-plane anisotropy [25]. As previously mentioned in our PNR measurements, we observed potential evidence of subtle, out-of-plane canting in the static magnetic state (with no spin pumping present), though the influence of this potential interaction on the FMR measurements is unclear as the FMR is performed in a dynamic state where spin pumping across the interface likely has a greater influence on the YIG film anisotropy. What is most compelling about our experimental data for this interpretation is not only the observed temperature dependence of the TSS-induced damping enhancement, but also the change in the temperature dependence of the resonance field shown in Fig. 4(d). The differential resonance field curve of the YIG/ $\text{Bi}_2\text{Te}_3$  and the YIG film shows a clear negative resonance field shift and with a stronger dependence below approximately 30 K, suggesting that this is linked to the suppression of the TI bulk conduction and the emergence of strong TSS, which also explains the damping enhancement at low temperature. Previous studies do not report such a strong temperature dependence at low temperature for the resonance field shift of the YIG/ $\text{Bi}_2\text{Se}_3$  compared to the YIG reference film [26,27]. In summary we observe significant modifications to the YIG magnetization dynamics due to the proximity to the TI film in the absence of possible confounding interfacial effects. Specifically, we observe significant spin pumping which increases at low temperatures and is accompanied by an additional in-plane anisotropy.

## V. CONCLUSIONS

To summarize, our BT/YIG system is uniquely suited to elucidate the intrinsic TI–MI magnetization dynamics due to the lack of (1) an extended transient layer in the

magnetic insulator at the magnetic insulator–substrate interface (confirmed in our previous work) [42], and the lack of (2) a low density, intergrowth region of the TI at the TI–magnetic insulator interface (confirmed here with our PNR results). Using temperature-dependent FMR, we found a strong damping enhancement at low temperature due to the TSS in the  $\text{Bi}_2\text{Te}_3$  film—a signature of significant spin pumping. Accompanying the damping enhancement, we also observed a large induced in-plane/easy-plane magnetic anisotropy for the BT/YIG heterostructure. We explain this by spin pumping and spin-momentum locking, due to which the precessing spins of the YIG are forced to align with the spins pumped into the TSS and therefore remain locked in the plane of the BT/YIG interface. The temperature dependence of the magnetotransport which supports the suppression of bulk conduction, and the emergence of WAL are consistent with the low-temperature enhanced spin pumping in the BT/YIG that we observed. Our PNR results did not provide direct evidence of a MPE in the BT/YIG system; however, we still observed an AHE-like signature at low temperatures, though this may be a spin Hall AHE, generated by interfacial scattering of spin currents, and not a MPE-induced AHE as previously reported in  $\text{Pt/CoFe}_2\text{O}_4$  [61]. Further study of TI/MI heterostructures is needed to assess their potential for unlocking a high-temperature, quantum anomalous Hall effect (QAHE) state [62–65]. To date, the QAHE state has been demonstrated via Proximity Induced Magnetization (PIM) in an all-telluride system of  $[\text{Zn}_{1-x}\text{Cr}_x\text{Te}/(\text{Bi}_y\text{Sb}_{1-y})_2\text{Te}_3/\text{Zn}_{1-x}\text{Cr}_x\text{Te}]$ , though the proximity-based exchange coupling facilitated by the Te-orbital overlap is significantly stronger than the proximity effect in TI/YIG [66], and here we did not directly measure any BT/YIG proximity effect. Additionally, TI/YIG interfacial band bending may complicate any potential QAHE state in TI/YIG systems [67,68].

#### ACKNOWLEDGMENTS

A.R.W.-C. and N.X.S. acknowledge financial support from NSF TANMS ERC under Award No. 1160504. A.R.W.-C. was supported by the National Defense Science and Engineering Graduate Fellowship of the Office of Naval Research. This material is based upon work supported by the U.S. Department of Energy, Office of Science, Office of Workforce Development for Teachers and Scientists, Office of Science

Graduate Student Research (SCGSR) program. The SCGSR program is administered by the Oak Ridge Institute for Science and Education (ORISE) for the DOE. ORISE is managed by ORAU under Contract No. DE-SC0014664. A portion of this research used resources at Sandia National Laboratories. Sandia National Laboratories is a multitechnology laboratory managed and operated by National Technology and Engineering Solutions of Sandia, LLC, a wholly owned subsidiary of Honeywell International Inc., for the U.S. Department of Energy’s National Nuclear Security Administration under Contract No. DE-NA0003525. This work was performed, in part, at the Center for Integrated Nanotechnologies, an Office of Science User Facility operated for the U.S. Department of Energy (DOE) Office of Science. A portion of this research used resources at the Spallation Neutron Source, a DOE Office of Science User Facility operated by the Oak Ridge National Laboratory. A.R.W.-C. and V.L. thank Haile Ambaye for his assistance during the setup of the PNR experiment. The work of C.D. was supported by the Deutsche Forschungsgemeinschaft (DFG, German Research Foundation) under Grant No. 271741898. The work of M.L. was supported by the German Bundesministerium für Wirtschaft und Energie (BMWi) under Grant No. 49MF180119. C.D. thanks O. Surzhenko for preliminary studies on FMR characterization of samples at room temperature and R. Meyer (INNOVENT e.V.) for their technical support. D.H. acknowledges partial support by the National Science Foundation under Grant No. DMR-1905662 and the Air Force Office of Scientific Research under Award No. FA9550-20-1-0247.

All opinions expressed in this paper are the author’s and do not necessarily reflect the policies and views of DOE, ORAU, or ORISE. This paper describes objective technical results and analysis. Any subjective views or opinions that might be expressed in the paper do not necessarily represent the views of the U.S. Department of Energy or the United States Government. Certain commercial equipment, instruments, software, or materials are identified in this paper in order to specify the experimental procedure adequately. Such identifications are not intended to imply recommendation or endorsement by NIST, nor it is intended to imply that the materials or equipment identified are necessarily the best available for the purpose. Additionally, any subjective views or opinions that might be expressed in the paper do not necessarily represent the views of NIST.

- 
- [1] M. Z. Hasan and C. L. Kane, *Rev. Mod. Phys.* **82**, 3045 (2010).
  - [2] J. E. Moore, *Nature (London)* **464**, 194 (2010).
  - [3] Y. Ando, *J. Phys. Soc. Jpn.* **82**, 102001 (2013).
  - [4] D. Hsieh, D. Qian, L. Wray, Y. Xia, Y. S. Hor, J. R. Cava, and M. Z. Hasan, *Nature (London)* **452**, 970 (2008).
  - [5] H. Zhang, C.-X. Liu, X.-L. Qi, X. Dai, Z. Fang, and S.-C. Zhang, *Nat. Phys.* **5**, 438 (2009).
  - [6] L. T. Dang, O. Breunig, Z. Wang, H. F. Legg, and Y. Ando, *Phys. Rev. Appl.* **20**, 024065 (2023).
  - [7] Y. Ando, T. Hamasaki, T. Kurokawa, K. Ichiba, F. Yang, M. Novak, S. Sasaki, K. Segawa, Y. Ando, and M. Shiraishi, *Nano Lett.* **14**, 6226 (2014).
  - [8] C. H. Li, O. M. J. van ’t Erve, C. Yan, L. Li, and B. T. Jonker, *Sci. Rep.* **8**, 10265 (2018).
  - [9] D. Hsieh, Y. Xia, D. Qian, L. Wray, J. H. Dil, F. Meier, J. Osterwalder, L. Patthey, J. G. Checkelsky, N. P. Ong, A. V. Fedorov, H. Lin, A. Bansil, D. Grauer, Y. S. Hor, R. J. Cava, and M. Z. Hasan, *Nature (London)* **460**, 1101 (2009).
  - [10] J. W. McIver, D. Hsieh, H. Steinberg, P. Jarillo-Herrero, and N. Gedik, *Nat. Nanotechnol.* **7**, 96 (2012).
  - [11] Q. Pan, Y. Liu, H. Wu, P. Zhang, H. Huang, C. Eckberg, X. Che, Y. Wu, B. Dai, Q. Shao, and K. L. Wang, *Adv. Electron. Mater.* **8**, 2200003 (2022).

- [12] M. De, R. Grassi, J.-Y. Chen, M. Jamali, D. Reifsnnyder Hickey, D. Zhang, Z. Zhao, H. Li, P. Quarterman, and Y. Lv, *Nat. Mater.* **17**, 800 (2018).
- [13] N. H. D. Khang, Y. Ueda, and P. N. A. Hai, *Nat. Mater.* **17**, 808 (2018).
- [14] I. M. Miron, K. Garello, G. Gaudin, P.-J. Zermatten, M. V. Costache, S. Auffret, S. Bandiera, B. Rodmacq, A. Schuhl, and P. Gambardella, *Nature (London)* **476**, 189 (2011).
- [15] L. Liu, O. J. Lee, T. J. Gudmundsen, D. C. Ralph, and R. A. Buhrman, *Phys. Rev. Lett.* **109**, 096602 (2012).
- [16] Y. Wang and H. Yang, *Acc. Mater. Res.* **3**, 1061 (2022).
- [17] X. Che, K. Murata, L. Pan, Q. L. He, G. Yu, Q. Shao, G. Yin, P. Deng, Y. Fan, B. Ma, X. Liang, B. Zhang, X. Han, L. Bi, Q. H. Yang, H. Zhang, and K. L. Wang, *ACS Nano* **12**, 5042 (2018).
- [18] S. Zhu, D. Meng, G. Liang, G. Shi, P. Zhao, P. Cheng, Y. Li, X. Zhai, Y. Lu, L. Chen, and K. Wu, *Nanoscale* **10**, 10041 (2018).
- [19] Z. Jiang, C. Z. Chang, C. Tang, P. Wei, J. S. Moodera, and J. Shi, *Nano Lett.* **15**, 5835 (2015).
- [20] C. Tang, C. Z. Chang, G. Zhao, Y. Liu, Z. Jiang, C. X. Liu, M. R. McCartney, D. J. Smith, T. Chen, and J. S. Moodera, *Sci. Adv.* **3**, e1700307 (2017).
- [21] X. Yao, B. Gao, M.-G. Han, D. Jain, J. Moon, J. Wook Kim, Y. Zhu, S.-W. Cheong, and S. Oh, *Nano Lett.* **19**, 4567 (2019).
- [22] S. Meyer, R. Schiltz, S. Geprägs, M. Opel, H. Huebl, R. Gross, and S. T. B. Goennenwein, *Appl. Phys. Lett.* **106**, 132402 (2015).
- [23] H. Nakayama, M. Althammer, Y.-T. Chen, K. Uchida, Y. Kajiwara, D. Kikuchi, T. Ohtani, S. Geprägs, M. Opel, S. Takahashi, R. Gross, G. E. W. Bauer, S. T. B. Goennenwein, and E. Saitoh, *Phys. Rev. Lett.* **110**, 206601 (2013).
- [24] Steven S.-L. Zhang and G. Vignale, *Phys. Rev. Lett.* **116**, 136601 (2016).
- [25] C. Tang, Q. Song, C.-Z. Chang, Y. Xu, Y. Ohnuma, M. Matsuo, Y. Liu, W. Yuan, Y. Yao, J. S. Moodera, S. Maekawa, W. Han, and J. Shi, *Sci. Adv.* **4**, eaas8660 (2018).
- [26] Y. T. Fanchiang, K. H. M. Chen, C. C. Tseng, C. C. Chen, C. K. Cheng, S. R. Yang, C. N. Wu, S. F. Lee, M. Hong, and J. Kwo, *Nat. Commun.* **9**, 223 (2018).
- [27] T. Liu, J. Kally, T. Pillsbury, C. Liu, H. Chang, J. Ding, Y. Cheng, M. Hilse, R. Engel-Herbert, A. Richardella, N. Samarth, and M. Wu, *Phys. Rev. Lett.* **125**, 017204 (2020).
- [28] M. Li, C.-Z. Chang, B. J. Kirby, M. E. Jamer, W. Cui, L. Wu, P. Wei, Y. Zhu, D. Heiman, J. Li, and J. S. Moodera, *Phys. Rev. Lett.* **115**, 087201 (2015).
- [29] F. Katmis, V. Lauter, F. S. Nogueira, B. A. Assaf, M. E. Jamer, P. Wei, B. Satpati, J. W. Freeland, I. Eremin, D. Heiman, P. Jarillo-Herrero, and J. S. Moodera, *Nature (London)* **533**, 513 (2016).
- [30] M. Li, Q. Song, W. Zhao, J. A. Garlow, T.-H. Liu, L. Wu, Y. Zhu, J. S. Moodera, M. H. W. Chan, G. Chen, and C.-Z. Chang, *Phys. Rev. B* **96**, 201301(R) (2017).
- [31] M. Mogi, T. Nakajima, V. Ukleev, A. Tsukazaki, R. Yoshimi, M. Kawamura, K. S. Takahashi, T. Hanashima, K. Kakurai, T.-H. Arima, M. Kawasaki, and Y. Tokura, *Phys. Rev. Lett.* **123**, 016804 (2019).
- [32] S. M. Suturin, A. M. Korovin, V. E. Bursian, L. V. Lutsev, V. Bourbina, N. L. Yakovlev, M. Montecchi, L. Pasquali, V. Ukleev, A. Vorobiev, A. Devishvili, and N. S. Sokolov, *Phys. Rev. Mater.* **2**, 104404 (2018).
- [33] A. Mitra, O. Cespedes, Q. Ramasse, M. Ali, S. Marmion, M. Ward, R. M. D. Byrdson, C. J. Kinane, J. F. K. Cooper, S. Langridge, and B. J. Hickey, *Sci. Rep.* **7**, 11774 (2017).
- [34] J. F. K. Cooper, C. J. Kinane, S. Langridge, M. Ali, B. J. Hickey, T. Niizeki, K. Uchida, E. Saitoh, H. Ambaye, and A. Glavic, *Phys. Rev. B* **96**, 104404 (2017).
- [35] C. L. Jermain, S. V. Aradhya, N. D. Reynolds, R. A. Buhrman, J. T. Brangham, M. R. Page, P. C. Hammel, F. Y. Yang, and D. C. Ralph, *Phys. Rev. B* **95**, 174411 (2017).
- [36] E. Shigematsu, Y. Ando, R. Oshima, S. Dushenko, Y. Higuchi, T. Shinjo, H. Jürgen von Bardeleben, and M. Shiraishi, *Appl. Phys. Express* **9**, 053002 (2016).
- [37] L. J. Riddiford, A. J. Grutter, T. Pillsbury, M. Stanley, D. Reifsnnyder Hickey, P. Li, N. Alem, N. Samarth, and Y. Suzuki, *Phys. Rev. Lett.* **128**, 126802 (2022).
- [38] Y. Lv, J. Kally, T. Liu, P. Quarterman, T. Pillsbury, B. J. Kirby, A. J. Grutter, P. Sahu, J. A. Borchers, M. Wu, N. Samarth, and J.-P. Wang, *Appl. Phys. Rev.* **9**, 011406 (2022).
- [39] C. Dubs, O. Surzhenko, R. Thomas, J. Osten, T. Schneider, K. Lenz, J. Grenzer, R. Hübner, and E. Wendler, *Phys. Rev. Mater.* **4**, 024416 (2020).
- [40] A. V. Chumak, P. Kabos, M. Wu, C. Abert, C. Adelman, A. O. Adeyeye, J. Åkerman, F. G. Alieve, A. Anane, and A. Awad, *IEEE Trans. Magn.* **58**, 1 (2022).
- [41] C. Dubs, O. Surzhenko, R. Linke, A. Danilewsky, U. Brückner, and J. Dellith, *J. Phys. D: Appl. Phys.* **50**, 204005 (2017).
- [42] A. R. Will-Cole, James L. Hart, Valeria Lauter, Alexander Grutter, Carsten Dubs, Morris Lindner, Timmy Reimann, Nichole R. Valdez, Charles J. Pearce, Todd C. Monson, Judy J. Cha, Don Heiman, and Nian X. Sun, *Phys. Rev. Mater.* **7**, 054411 (2023).
- [43] See Supplemental Material at <http://link.aps.org/supplemental/10.1103/PhysRevMaterials.8.074409> for additional data and information pertaining to the structural film quality, magnetotransport behavior, static and dynamic magnetic behavior.
- [44] V. Lauter, H. Ambaye, R. Goyette, W.-T. Hal Lee, and A. Parizzi, *Phys. B (Amsterdam, Neth.)* **404**, 2543 (2009).
- [45] V. Lauter-Pasyuk, *Collecti. SFN* **7**, s221 (2007).
- [46] V. Lauter, H. J. C. Lauter, A. Glavic, and B. P. Toperverg, Reflectivity, off-specular scattering, and GISANS neutrons, *Reference Module in Materials Science and Materials Engineering* (Elsevier, 2016).
- [47] D. Reifsnnyder Hickey, J. G. Azadani, A. R. Richardella, J. C. Kally, J. S. Lee, H. Chang, T. Liu, M. Wu, N. Samarth, T. Low, and K. A. Mkhoyan, *Phys. Rev. Mater.* **3**, 061201(R) (2019).
- [48] P.-Y. Chuang, S.-H. Su, C.-W. Chong, Y.-F. Chen, Y.-H. Chou, J.-C.-A. Huang, W.-C. Chen, C.-M. Cheng, K.-D. Tsuei, C.-H. Wang, Y.-W. Yang, Y.-F. Liao, S.-C. Weng, J.-F. Lee, Y.-K. Lan, S.-L. Chang, C.-H. Lee, C.-K. Yang, H.-L. Su, and Y. Wu, *RSC Adv.* **8**, 423 (2018).
- [49] A.-M. Netsou, D. Muzychenko, H. Dausy, T. Chen, F. Song, K. Schouteden, M. Van Bael, and C. Van Haesendonck, *ACS Nano* **14**, 13172 (2020).
- [50] L. Locatelli, A. Kumar, P. Tsipas, A. Dimoulas, E. Longo, and R. Mantovan, *Sci. Rep.* **12**, 3891 (2022).
- [51] J. Wang, A. M. DaSilva, C.-Z. Chang, K. He, J. K. Jain, N. Samarth, X.-C. Ma, Q.-K. Xue, and M. H. W. Chan, *Phys. Rev. B* **83**, 245438 (2011).

- [52] A. Kandala, A. Richardella, D. Rench, D. Zhang, T. Flanagan, and N. Samarth, *Appl. Phys. Lett.* **103**, 202409 (2013).
- [53] S.-Y. Huang, C.-W. Chong, Y. Tang, T.-C. Chen, K.-C. Wu, M.-K. Lee, J.-C.-A. Huang, Z. Li, and H. Qiu, *Sci. Rep.* **7**, 2422 (2017).
- [54] P. Li, J. Ding, S. S.-L. Zhang, J. Kally, T. Pillsbury, O. G. Heiononen, G. Rimal, C. Bi, A. DeMann, S. B. Field, W. Wang, J. Tang, J. S. Jiang, A. Hoffmann, N. Samarth, and M. Wu, *Nano Lett.* **21**, 84 (2021).
- [55] V. H. Ortiz, M. Aldosary, J. Li, Y. Xu, M. I. Lohmann, P. Sellappan, Y. Kodera, J. E. Garay, and J. Shi, *APL Mater.* **6**, 121113 (2018).
- [56] M. Lang, M. Montazeri, M. C. Onbasli, X. Kou, Y. Fan, P. Upadhyaya, K. Yao, F. Liu, Y. Jiang, W. Jiang, K. L. Wong, G. Yu, J. Tang, T. Nie, L. He, R. N. Schwartz, Y. Wang, C. A. Ross, and K. L. Wang, *Nano Lett.* **14**, 3459 (2014).
- [57] P. Li *et al.*, *Sci. Adv.* **5**, eaaw3415 (2019).
- [58] Z. Jiang, C.-Z. Chang, C. Tang, J.-G. Zheng, J.-G. Zheng, J. Moodera, and J. Shi, *AIP Adv.* **6**, 055809 (2016).
- [59] Y.-T. Chen, S. Takahashi, H. Nakayama, M. Althammer, S. Goennenwein, E. Saitoh, and G. Bauer, *Phys. Rev. B* **87**, 144411 (2013).
- [60] H. Wang, J. Kally, C. Sahin, T. Liu, W. Yanez, E. J. Kamp, A. Richardella, M. Wu, M. E. Flatté, and N. Samarth, *Phys. Rev. Res.* **1**, 012014(R) (2019).
- [61] W. Amamou, I. V. Pinchuk, A. H. Trout, R. E. A. Williams, N. Antolin, A. Goad, D. J. O'Hara, A. S. Ahmed, W. Windl, D. W. McComb, and R. K. Kawakami, *Phys. Rev. Mater.* **2**, 011401(R) (2018).
- [62] C.-X. Liu, S.-C. Zhang, and X.-L. Qi, *Annu. Rev. Condens. Matter. Phys.* **7**, 301 (2016).
- [63] R. Yu, W. Zhang, H.-J. Zhang, S.-C. Zhang, X. Dai, and Z. Fang, *Science* **329**, 61 (2010).
- [64] Y. L. Chen, J.-H. Chu, J. G. Analytis, Z. K. Liu, K. Igarashi, H.-H. Kuo, X. L. Qi, S. K. Mo, R. G. Moore, D. F. Lu, M. Hashimoto, T. Sasagawa, S. C. Zhang, I. R. Fisher, Z. Hussain, and Z. X. Shen, *Science* **329**, 659 (2010).
- [65] A. J. Grutter and Q. L. He, *Phys. Rev. Mater.* **5**, 090301 (2021).
- [66] R. Watanabe, R. Yoshimi, M. Kawamura, M. Mogi, A. Tsukazaki, X. Z. Yu, K. Nakajima, K. S. Takahashi, M. Kawasaki, and Y. Tokura, *Appl. Phys. Lett.* **115**, 102403 (2019).
- [67] W. Luo and X.-L. Qi, *Phys. Rev. B* **87**, 085431 (2013).
- [68] G. Qiu, H.-Y. Yang, S. Kong Chong, Y. Cheng, L. Tai, and K. L. Wang, *Nanomaterials* **13**, 2655 (2023).